Exp Fluids (2007) 43:655–664
DOI 10.1007/s00348-007-0315-1

RESEARCH ARTICLE

A potential-flow, deformable-body model for fluid–structure interactions with compact vorticity: application to animal swimming measurements

Jifeng Peng · John O. Dabiri

Received: 12 February 2007 / Revised: 3 April 2007 / Accepted: 13 April 2007 / Published online: 8 August 2007

Abstract This paper presents an approach to quantify the unsteady fluid forces, moments and mass transport generated by swimming animals, based on measurements of the surrounding flow field. These goals are accomplished within a framework that is independent of the vorticity field, making it unnecessary to directly resolve boundary layers on the animal, body–vortex interactions, or interactions among vortex lines in the wake. Instead, the method identifies Lagrangian coherent structures in the flow, whose dynamics in flows with compact vorticity are shown to be well approximated by potential flow concepts, especially the Kirchhoff and deformation potentials from deformable body theory. Examples of the application of these methods are given for pectoral fin locomotion of the bluegill sunfish and undulatory swimming of jellyfish, and the methods are validated by analysis of a canonical starting vortex ring flow. The transition to a Lagrangian approach toward animal swimming measurements suggests the possibility of implementing recently developed particle tracking (vis-à-vis DPIV) techniques for fully three-dimensional measurements of animal swimming.

J. Peng · J. O. Dabiri
Department of Bioengineering,
California Institute of Technology,
Pasadena, CA 91125, USA

J. O. Dabiri (✉)
Graduate Aeronautical Laboratories,
California Institute of Technology,
Pasadena, CA 91125, USA
e-mail: jodabiri@caltech.edu

1 Introduction

A distinguishing feature of animal swimming in real fluids is the generation of vorticity and the shedding of vortices into the wake. It is for this reason that much of the experimental work on animal swimming has been approached from a perspective that aims to quantify vorticity dynamics (e.g. Drucker and Lauder 1999, 2001; Wilga and Lauder 2004; Bartol et al. 2005; Dabiri et al. 2005; Stamhuis and Nauwelaerts 2005). The standard tool for flow field measurements is digital particle image velocimetry (DPIV), which quantifies the velocity field of the flow in an Eulerian frame of reference, i.e. instantaneously and at fixed locations in space. The vorticity field is then immediately deduced by numerically taking the curl of the measured velocity field.

These wake studies have been complemented by theoretical tools that, in principle, enable the quantification of instantaneous forces and moments created by the animal, given knowledge of the surrounding flow field. However, with the exception of purely steady flows, these methods require either measurement of the boundary layers on the animal, the replacement of the animal body with an equivalent system of image vorticity, or measurements on the surface of a control volume with length scales an order of magnitude larger than the animal itself (Wu 1981; Noca 1997, 1999). Each of these options is difficult to achieve in practice. Therefore, the state-of-the-art in the field is the calculation of time-averaged forces, in which unsteady effects like added-mass tend to cancel when integrated over a swimming cycle (Daniel 1984).

The study of body–vortex interactions, such as those occurring due to incident vortices from upstream or generated by the head of the animal (e.g. Gopalkrishnan et al. 1994; Liao et al. 2003; Beal et al. 2006), is also

limited by practical obstacles to quantitative flow visualization. The velocity and vorticity fields cannot usually be well resolved at the interface between the animal and the surrounding fluid while maintaining a full-field view of the flow (see Anderson et al. 2001, for a notable exception). Together these limitations represent a potential show-stopper to more detailed and quantitative analyses of animal swimming.

In general, the challenge of analyzing flow measurements is related to the need to identify consistent boundaries in the flow on which to evaluate the equations of motion. The aforementioned theoretical tools rely on either the fluid–solid boundary represented by the animal surface, or a virtual, fluid–fluid boundary used to define a control volume. Recent applications of Lagrangian, particle-tracking flow analyses have demonstrated that in many unsteady flows there exist physically meaningful, fluid–fluid boundaries that act as barriers to fluid transport. The Lagrangian coherent structures (LCS) defined by these real fluid–fluid boundaries are currently studied for their kinematic properties and have been used primarily to better understand transport and mixing processes or to identify fluid structures in turbulence (e.g. Haller 2000, 2001, 2002; Green et al. 2006).

This paper examines the dynamic properties of LCS and shows that these properties can be used to deduce the forces and moments on a swimming animal. A distinguishing feature of this approach is that it does not appeal to the vorticity dynamics in the flow. Instead, it is shown that potential flow concepts from deformable body theory can be used to approximate the LCS dynamics when the vorticity field is sufficiently compact (i.e. bounded spatially). The LCS tend to appear away from the surface of the animal body but not at prohibitively large distances away. Together these properties make it possible to determine instantaneous, unsteady forces and moments created by swimming animals without the need to resolve boundary layers on the animal, to construct equivalent image vorticity systems, or to use far-field control volume analyses. In addition, the known transport properties of LCS enable quantification of mass transport that is induced by the animal during locomotion.

Recent implementation of these methods in studies of the bluegill sunfish pectoral fin and the entire body of a free-swimming jellyfish are highlighted to demonstrate the capabilities and limitations of the present approach. To be sure, the methods presented here are more generally applicable than animal swimming. However, the study of animal swimming provides a robust test of the method in flows characterized by unsteady fluid–structure interactions and complex vorticity dynamics. Validation using direct numerical simulations of a starting vortex ring formed by a piston-cylinder apparatus demonstrates the capabilities of the method in a more canonical flow and helps to put these results in the context of traditional fluid mechanics analyses.

Section 2 presents the experimental and analytical methods that constitute this vorticity-free approach to the study of animal swimming. Examples of the resulting measurements, taken from recent contributions by the authors and coworkers, are presented in Sect. 3 along with a validation of the method using direct numerical simulations of vortex ring formation by a piston-cylinder apparatus. Finally, Sect. 4 suggests a path forward that addresses issues such as three-dimensional flow, in situ animal measurements, and measurement validation.

2 Experimental and analytical methods

2.1 Identification of Lagrangian coherent structures

The first step in the vorticity-free approach to swimming measurements is to identify the LCS from which fluid dynamic forces and moments will be deduced. Haller (2001) and Shadden et al. (2005, 2006) identify LCS as ridges of local maxima in the finite-time Lyapunov exponent (FTLE) field of a given flow. The FTLE measures the maximum linearized growth rate of the distance between initially adjacent fluid particles. To determine this quantity, fluid particles are tracked over a finite time interval. Since the available information regarding the velocity field $\mathbf{u}$ is typically given in an Eulerian frame (e.g. DPIV), the particle trajectories $\mathbf{x}(t)$ are determined by numerical solution of the ordinary differential equation

$$\dot{\mathbf{x}}(t) = \mathbf{u}(\mathbf{x}(t), t), \tag{1}$$

with the initial position of the fluid particle used as the initial condition. The flow map, which maps fluid particles from their initial location at time t_0 to their location at time $t_0 + T$ can be expressed as

$$\varphi_{t_0}^{t_0+T}(\mathbf{x}) : \mathbf{x}(t_0) \rightarrow \mathbf{x}(t_0 + T), \tag{2}$$

where $\varphi_{t_0}^{t_0+T}(\mathbf{x}) = \mathbf{x}(t_0 + T)$ describes the current location of a fluid particle advected from the location $\mathbf{x}(t_0)$ at time t_0 after a time interval T. A given infinitesimal perturbation $\delta\mathbf{x}_0$ (i.e. fluid particle separation) at time t_0 is transformed to $\delta\mathbf{x}$ by the relation

$$\delta\mathbf{x} = \nabla\varphi_{t_0}^{t_0+T}(\mathbf{x})\delta\mathbf{x}_0, \tag{3}$$

where $\nabla\varphi_{t_0}^{t_0+T}(\mathbf{x})$ is the deformation gradient tensor and defined by

$$\nabla \varphi_{t_0}^{t_0+T}(\mathbf{x}) = \frac{d\varphi_{t_0}^{t_0+T}(\mathbf{x})}{d\mathbf{x}}. \tag{4}$$

The magnitude of the mapped perturbation is defined by the symbol $\|\delta\mathbf{x}\|$ and given by

$$\|\delta\mathbf{x}\| = \sqrt{\langle \delta\mathbf{x}_0, [\nabla\varphi(\mathbf{x})]^* \nabla\varphi(\mathbf{x})\delta\mathbf{x}_0\rangle}, \tag{5}$$

where [ ]* denotes the transpose of matrix [ ]. The inner product can be written in summation form as

$$\begin{aligned}&\langle \delta\mathbf{x}_0, [\nabla\varphi(\mathbf{x})]^* \nabla\varphi(\mathbf{x})\delta\mathbf{x}_0\rangle \\ &\quad = \sum_i \sum_j \sum_k (\delta\mathbf{x}_0)_i ([\nabla\varphi(\mathbf{x})]^*)_{ik} (\nabla\varphi(\mathbf{x}))_{kj} (\delta\mathbf{x}_0)_j\end{aligned} \tag{6}$$

Let the symmetric matrix Δ be defined as the Cauchy–Green deformation tensor:

$$\Delta = [\nabla \varphi_{t_0}^{t_0+T}(\mathbf{x})]^* \nabla \varphi_{t_0}^{t_0+T}(\mathbf{x}), \tag{7}$$

and let $\lambda_{\max}(\Delta)$ be the maximum eigenvalue of the Cauchy–Green deformation tensor. Note from Eq. 5 that $\sqrt{\lambda_{\max}(\Delta)}$ gives the maximum stretching of $\delta\mathbf{x_0}$ (i.e. the maximum separation of fluid particle pairs initially located at $\mathbf{x}(t_0)$) when $\delta\mathbf{x_0}$ is aligned with the eigenvector associated with $\lambda_{\max}(\Delta)$; hence

$$\|\delta\mathbf{x}\|_{\max} = \sqrt{\lambda_{\max}(\Delta)}\|\delta\mathbf{x}_0\|. \tag{8}$$

The finite-time Lyapunov exponent $\sigma_t^T(\mathbf{x})$ is then defined as:

$$\sigma_t^T(\mathbf{x}) = \frac{1}{|T|}\ln\sqrt{\lambda_{\max}(\Delta)} = \frac{1}{|T|}\ln\left\|\frac{\delta\mathbf{x}(T)}{\delta\mathbf{x}(0)}\right\|. \tag{9}$$

Shadden et al. (2005) showed that the ridges of local maxima in the FTLE field act as material lines in the flow and, furthermore, are nearly perfect barriers to fluid transport when computed in the limit as T becomes very large. Shadden et al. (2005) also derived an estimate for the fluid flux across an LCS that is deduced from finite-time data (i.e. finite T in Eq. 9) and showed that, for practical purposes, this quantity is often negligible. Hence, the LCS are treated as ideal material lines in practice. The absolute value $|T|$ is used instead of T in Eq. 8 because FTLE can be computed for $T > 0$ and $T < 0$. The material line is called a repelling LCS ($T > 0$) over the time interval if infinitesimal perturbations away from this line grow monotonically under the linearized flow. The material line is called an attracting LCS ($T < 0$) if it is a repelling LCS over the interval in backward time. In the parlance of dynamical systems, repelling and attracting LCS reveal stable and unstable manifolds, respectively.

The FTLE field can be calculated from a time-series of discrete velocity field data typical of DPIV measurements. The flow map is determined by integration of the velocity field and the FTLE can be calculated from the flow map. There are currently at least two software packages available for the calculation of FTLE fields from DPIV-type velocity field data. MANGEN, a package developed by F. Lekien and C. Coulliette, is a C-language program previously implemented by Shadden et al. (2005, 2006) and is available for download at http://www.lekien.com/~francois/software. A MATLAB package for FTLE calculation has been developed by the authors (Peng and Dabiri 2007) and is available for download at http://dabiri.caltech.edu/software.

The extraction of LCS curves from FTLE fields can be accomplished by a variety of ad hoc methods including thresholding or gradient searches of the FTLE field to identify local maxima. Shadden (2006) derives more rigorous criteria than these; however, for practical purposes, identification of LCS boundaries from well-resolved FTLE fields is relatively insensitive to the implemented method of extraction.

Figure 1 shows the forward-time and the backward-time FTLE fields computed for a steadily propagating vortex ring generated by a piston-cylinder apparatus (Shadden et al. 2006). The corresponding repelling and attracting LCS identified by the ridges of high FTLE values are shown in Fig. 2. The increasingly sinuous nature of the repelling (attracting) LCS near the front (rear) of the vortex ring is the result of perturbations from an ideal, unperturbed vortex

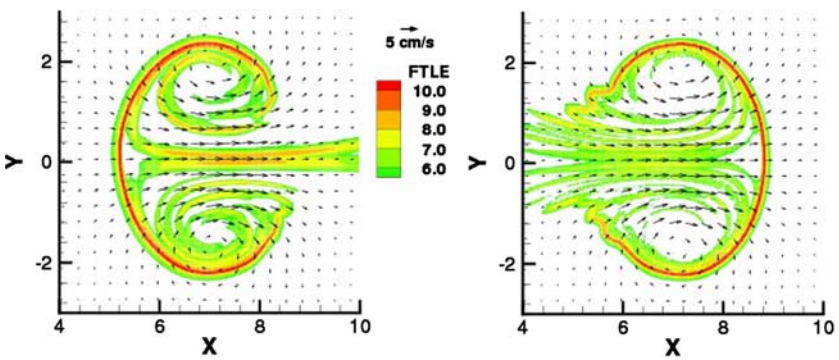

Fig. 1 Contour plot of forward-time (*left*) backward-time (*right*) FTLE fields for vortex ring propagating from *left* to *right*. LCS are identified by the ridge of high FTLE values (*red*)

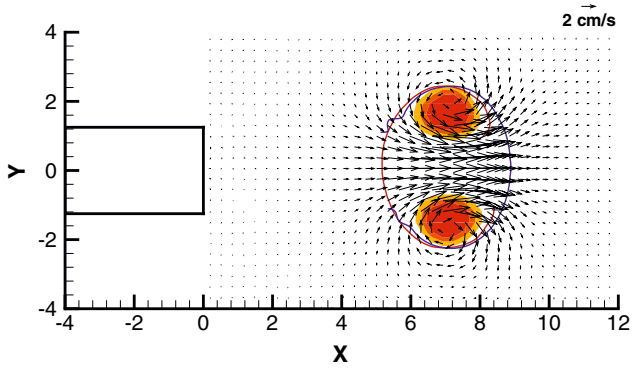

Fig. 2 Vortex ring generated by piston-cylinder apparatus. Vortex ring propagates from *left* to *right*. *Red curve*, forward-time LCS; *blue curve*, backward-time LCS; *filled contours*, vorticity magnitude; *black rectangle*, outline of downstream end of cylinder

ring configuration with connected stable and unstable manifolds (i.e. connected streamlines emanating from the rear and front stagnation points, respectively; see Shadden et al. 2006). Increasing detail of this sinuous structure is revealed with increasing integration time $|T|$.

2.2 The potential flow hypothesis

Given the geometry and kinematics of the LCS in the flow, we aim to use these structures to deduce dynamics (i.e. forces and moments) of the corresponding flow field. The present method takes advantage of the fact that the LCS represents a slip boundary in the flow on which a no through-flow condition holds, since the LCS is a material line. If we hypothesize that the shear stresses on and outside the LCS boundary are negligible, then the flow external to the LCS can be solved as a linear homogenous boundary value problem with nonhomogenous boundary conditions, i.e. a solution of Laplace's equation for the velocity potential ϕ.

The potential flow hypothesis is valid, for example, when all of the vorticity in the flow is enclosed by the LCS, as in the isolated vortex ring flow shown in Fig. 2 (Shadden et al. 2006). If the potential flow hypothesis holds, we can immediately make use of existing theory for the dynamics of deformable bodies in potential flow in order to deduce the forces and moments on the LCS. These forces and moments can be related unambiguously to the dynamics of the animal in the flow. The following section outlines the governing equations of motion.

2.3 Equations of motion

Galper and Miloh (1995) have previously derived the equations of motion for a deformable body in an arbitrary potential flow field. We make direct use of these equations presently, where the LCS structure is treated as a deformable body. It is important to note that there exist no a priori restrictions on which segments of the repelling and attracting LCS can be used to construct the deformable body, as long as (1) the segments form a closed curve and (2) the aforementioned potential flow hypothesis is satisfied. Nonetheless, certain combinations of the LCS provide more information regarding the fluid dynamics than others; hence, the choice should be made judiciously (see next section).

Let $\mathbf{U}_1 = \nabla\phi_1(\mathbf{X}, t)$ represent the ambient flow field surrounding the LCS, where ϕ_1 is the velocity potential of the ambient flow and $\mathbf{X}$ is the position vector measured relative to the laboratory frame of reference. The outward-facing unit normal to the LCS is denoted $\mathbf{n}$; the position vector relative to the LCS centroid, $\mathbf{x}$; and the instantaneous surface of the LCS, $S(\mathbf{x}, t) = 0$. The velocity potential that arises due to the presence of the LCS in the flow is given by

$$\phi_2 = \mathbf{U}_2 \cdot \mathbf{\Phi} + \mathbf{\Omega} \cdot \mathbf{\Psi} + \phi_d + \phi_0 \tag{10}$$

where $\mathbf{U}_2$ is the linear velocity of the LCS centroid in the laboratory frame and $\mathbf{\Omega}$ is the angular velocity of the principal axes of the LCS. The harmonic functions $\mathbf{\Phi}, \mathbf{\Psi}, \phi_d$, and ϕ_0 represent, respectively, the translational Kirchhoff potential, rotational Kirchhoff potential, deformation potential, and additional potential associated with the ambient flow. These potentials satisfy the boundary conditions listed below:

$$\frac{\partial\mathbf{\Phi}}{\partial n} = \mathbf{n}|_S; \quad \frac{\partial\mathbf{\Psi}}{\partial n} = \mathbf{x}\times\mathbf{n}|_S; \quad \frac{\partial\phi_d}{\partial n} = -\frac{\partial S/\partial t}{|\nabla S|}\Big|_S; \quad \frac{\partial\phi_0}{\partial n} = -\mathbf{U}_1\cdot\mathbf{n}|_S \tag{11}$$

where each is evaluated on the LCS surface $S(t)$. In addition, $\phi_2 \to 0$ as $|\mathbf{x}| \to \infty$. The fluid dynamic force $\mathbf{F}$ and moment $\mathbf{M}$ (per unit fluid density) acting on the LCS are given by

$$\mathbf{F} = \frac{\mathrm{d}}{\mathrm{d}t}\int_S \phi\mathbf{n}\,\mathrm{d}S - \int_S \nabla\phi(\nabla\phi\cdot\mathbf{n})\mathrm{d}S + \frac{1}{2}\int_S (\nabla\phi)^2\mathbf{n}\,\mathrm{d}S \tag{12}$$

$$\begin{aligned}\mathbf{M} = {} & \frac{\mathrm{d}}{\mathrm{d}t}\int_S \phi\mathbf{x}\times\mathbf{n}\,\mathrm{d}S + \mathbf{U}_2 \\ & \times\int_S \phi\mathbf{n}\,\mathrm{d}S - \int_S \mathbf{x}\times\mathbf{U}_1(\nabla\phi\cdot\mathbf{n})\mathrm{d}S \\ & + \frac{1}{2}\int_S (\nabla\phi)^2(\mathbf{x}\times\mathbf{n})\mathrm{d}S\end{aligned} \tag{13}$$

where $\phi = \phi_1 + \phi_2$. The following sections consider the application of these governing equations to two common classes of animal swimming measurements in which we will assume that ambient flow and LCS rotation are negligible, i.e. $\mathbf{U}_1 = \mathbf{\Omega} = \phi_0 = 0$.

2.3.1 Inertial frame; single appendage measurements

When studying the dynamics of single appendages in an inertial frame, we must account for the combined dynamical effect of the appendage and the vorticity that it generates. The LCS captures this by delineating an 'effective appendage' boundary that interacts with irrotational fluid surrounding the appendage–vortex system. Specifically, the effective appendage is given by the closed boundary formed by the intersection of the forward- and backward-time LCS curves (cf. Figs. 1 and 2). If the deformation of the effective appendage is small relative to its translation through the fluid, i.e. $\phi_d << \mathbf{U}_2 \cdot \mathbf{\Phi}$, then Eq. 12 reduces to

$$\mathbf{F} = \frac{\mathrm{d}}{\mathrm{d}t}\int_S (\mathbf{U}_2 \cdot 2\mathbf{\Phi})\mathbf{n}\,\mathrm{d}S \tag{14}$$

The balance of this fluid dynamic force and the external force $\mathbf{F}_{\text{ext}}$ applied by the animal to the appendage leads to a temporal change in the momentum of the effective appendage:

$$\mathbf{F} + \mathbf{F}_{\text{ext}} = \frac{\mathrm{d}}{\mathrm{d}t}(V_{\text{LCS}}\mathbf{U}_2) \tag{15}$$

or, equivalently,

$$\frac{\mathrm{d}}{\mathrm{d}t}(V_{\text{LCS}}(\mathbf{I} + \mathbf{A}_{\text{LCS}})\mathbf{U}_2) = \mathbf{F}_{\text{ext}} \tag{16}$$

where V_{LCS} is the volume of fluid displaced by the LCS, $\mathbf{I}$ is the identity matrix, and $\mathbf{A}_{\text{LCS}}$ is the added-mass tensor of the LCS (i.e. $\mathbf{A}_{\text{LCS}} = -\int_S \mathbf{\Phi} \cdot \mathbf{n}\,\mathrm{d}S$; Lamb 1932). Since the external force $\mathbf{F}_{\text{ext}}$ is applied by the animal, an equal and opposite locomotive force $\mathbf{F}_{\text{L}}$ is exerted by the fluid on the animal, i.e. $\mathbf{F}_{\text{L}} = -\mathbf{F}_{\text{ext}}$.

2.3.2 Non-inertial frame; whole animal measurements

It is often necessary to measure animal swimming in a non-inertial frame; for example, when tracking free-swimming animals over distances longer than a stationary measurement window will permit. In these cases, the LCS centroid velocity $\mathbf{U}_2$ in Eq. 10 cannot be determined by visual inspection. However, if a closed curve surrounding the entire animal body can be constructed from the measured LCS, then the locomotive force generated at the animal–fluid interface becomes an internal force in the system and Eq. 12 reduces to a simplified expression for $\mathbf{U}_2$:

$$\frac{\mathrm{d}}{\mathrm{d}t}\left[V_{\text{LCS}}(\mathbf{I} + \mathbf{A}_{\text{LCS}})\mathbf{U}_2 - \int_S \phi_d \mathbf{n}\,\mathrm{d}S\right] = 0 \tag{17}$$

The deformation potential ϕ_d can be determined by using a standard boundary value problem solver (e.g. MATLAB) with the boundary condition specified in Eq. 11. The problem then becomes purely kinematic, in which the animal body velocity $\mathbf{U}_{\text{body}}$ can be deduced from its weighted contribution to the velocity of the LCS centroid, i.e.

$$\mathbf{U}_{\text{body}} = \frac{\mathbf{U}_2 V_{\text{LCS}} - \mathbf{U}_{\text{fluid}} V_{\text{fluid}}}{V_{\text{body}}} \tag{18}$$

where V_{body} is the volume of the animal body (assumed neutrally buoyant), and the subscript fluid refers to properties of the fluid enclosed by the LCS.

It is important to note that, unlike the previous section in which deformation of the effective appendage was neglected, whole body calculations based primarily on either the repelling or attracting LCS can have a substantial contribution from the deformation potential ϕ_d in Eq. 17. This is because the lobular portions of the LCS may be included in the deformable body in these cases. In the previous section, the deforming, lobular portions of both the repelling and attracting LCS were eliminated from the analysis when the LCS were intersected to determine the effective appendage boundary.

3 Results

3.1 Bluegill sunfish pectoral fin locomotion

The analysis presented in Sect. 2.3.1 was applied by Peng et al. (2007) to DPIV measurements of the bluegill sunfish pectoral fin. The animals were swum in a flume so that they could be observed in an inertial frame of reference. Since measurements were taken in a transverse plane, i.e. with ambient flow normal to the measurement plane, Eq. 16 could be used to deduce the lateral and lift components of the locomotive force $\mathbf{F}_{\text{L}}$ (but not the thrust component). Figure 3 shows a snapshot of the computed forward- and backward-time FTLE fields and the resulting LCS structure that comprises the effective appendage boundary. These FTLE fields are not resolved as sharply as the vortex ring calculations shown in Fig. 1. This is due to the shorter integration time $|T|$, the result of a shorter duration of available DPIV measurements. Nonetheless, the effective appendage is reconstructed without much difficulty.

Figure 4 plots the measured lateral and lift forces deduced from the vorticity-free analysis. For comparison, the steady force level determined using the vorticity method of Drucker and Lauder (1999) is also plotted. The time-averaged force computed using the vorticity method is sensitive to the time at which the vorticity field is evaluated and the vorticity threshold used to identify the spatial extent of the shed vortex. We selected an instant near the end of the fin downstroke and included all vorticity above the background noise level in the calculation. The result is provided for qualitative comparison with the present vorticity-free method. As shown in Fig. 4, the present method provides detailed information regarding the transient fluid dynamic forces, in addition to the time-averaged dynamics. To be sure, this particular data set is limited by a lack of measurement data before the start of the fin downstroke at time $t = 0$. Hence, at the beginning of the fin motion there is insufficient data to compute the backward-time FTLE and the corresponding repelling LCS, which locates the front boundary of the effective appendage. Since it is not possible to evaluate the locomotive forces until this portion of the effective appendage geometry is revealed, the peak force generation during the early downstroke is not captured in the analysis and the corresponding time-averaged force over the downstroke may be underestimated. Nevertheless, the transient force dynamics that are captured agree with observations of instantaneous animal body kinematics (Peng et al. 2007).

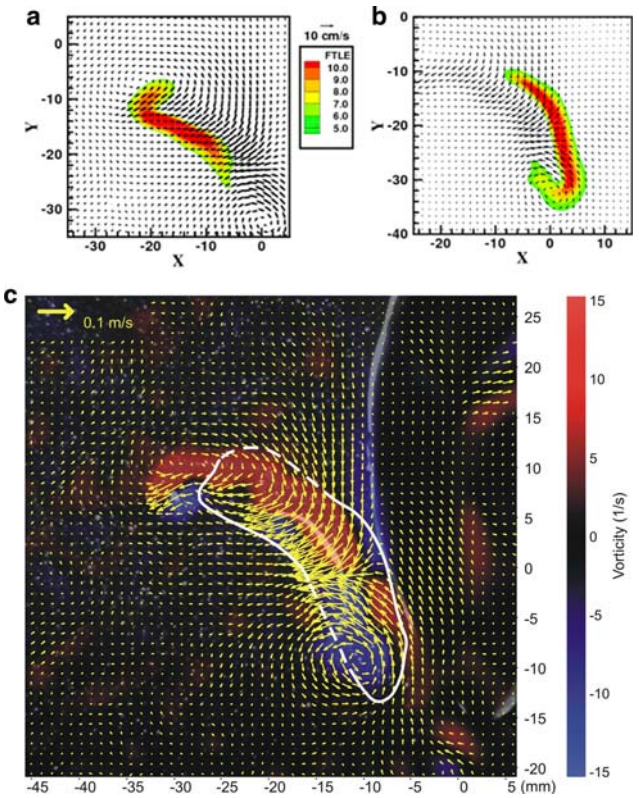

Fig. 3 FTLE fields and LCS for the flow generated by a bluegill sunfish pectoral fin. **a** Backward-time FTLE field; **b** forward-time FTLE field. Position coordinates are specified in millimeters. **c** Boundary of the effective appendage derived from the repelling and attracting LCS. *Solid curves* on the *left* and *right* show the attracting and repelling LCS, respectively. *Broken curves* are splines connecting the LCS. The fin (the curved feature with high brightness inside the LCS curves) can be seen embedded inside the effective appendage

3.2 Jellyfish undulatory locomotion

The analysis presented in Sect. 2.3.2 was applied to DPIV measurements of free-swimming *Aurelia aurita* medusae

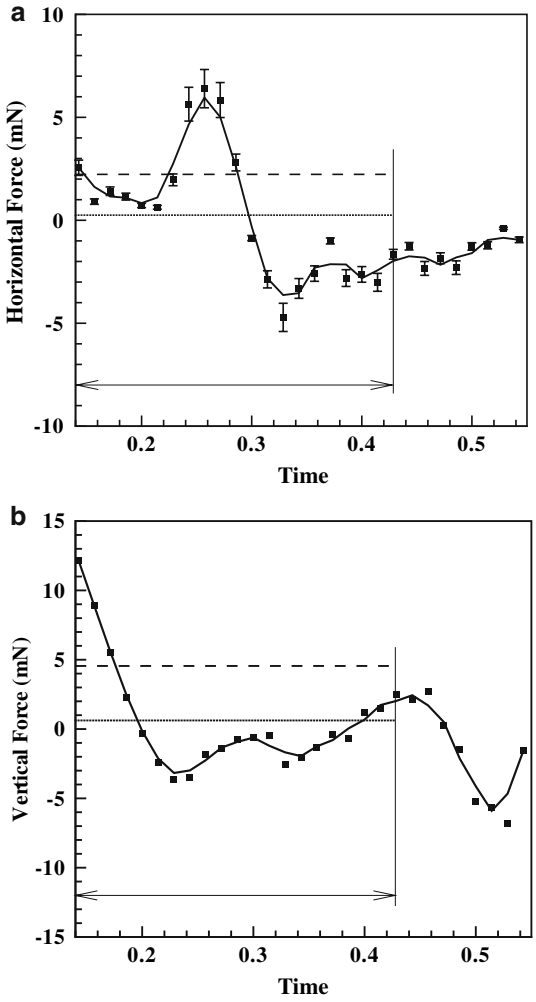

Fig. 4 Measured locomotive forces in **a** horizontal and **b** vertical directions. Time is normalized by the duration of the fin stroke cycle. *Squares*: vorticity-free method. *Error bars* indicate uncertainty from measurement and evaluation. For comparison, the steady horizontal and vertical force levels determined using the vorticity method of Drucker and Lauder (1999) are shown in *dashed lines*, and the time average of the instantaneous data over the same interval is given by the *solid horizontal lines*. The interval over which the time averages are taken is indicated by the *arrows*

(i.e. jellyfish). This species of jellyfish swims via full body undulations that create vortex rings of alternating rotational orientation during the swimming cycle (Dabiri et al. 2005). The animals were observed in an inertial frame in order to validate the non-inertial analytical methods. Figure 5 shows a snapshot of the forward-time LCS structure. Deformation of the lobular portions of the LCS (i.e., the two elongated lobes) upstream of the animal makes a substantial contribution to Eq. 17. Figure 6 compares the measured LCS centroid velocity $\mathbf{U}_2(t)$ to that predicted by Eq. 17; the agreement is reasonable, and it appears that the discrepancies are due to three-dimensional flow effects that cannot be captured by the two-dimensional DPIV measurements.

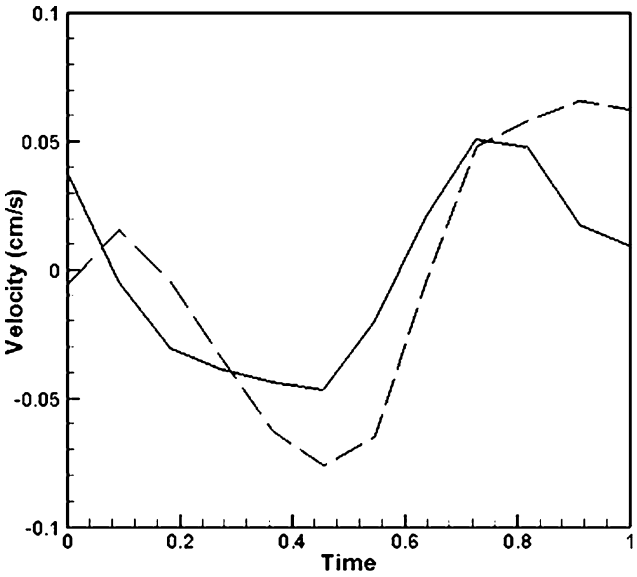

Fig. 6 Velocity of the LCS surrounding a free-swimming jellyfish. *Solid line*: directly measured velocity of the LCS; *dashed line*: vorticity-free method. Velocity is plotted as the instantaneous velocity minus the average velocity over the swimming cycle. Time is normalized by the duration of the swimming cycle

3.3 Validation of the potential flow hypothesis

To test the potential flow hypothesis and associated analytical method, we analyzed direct numerical simulations of vortex ring formation by a piston-cylinder apparatus. Details of the numerical model, which is similar to the experiment shown in Fig. 2, are described in a separate study (Shadden et al. 2007). The forward-time FTLE fields are shown for four frames in Fig. 7. The LCS extracted from the forward- and backward-time FTLE fields are plotted in Fig. 8, showing the temporal evolution of the flow. As in the case of the bluegill sunfish pectoral fin data, the backward-time LCS structure could not be identified until a finite time after flow initiation, since no data exists before that time. In Fig. 9, the total fluid momentum determined by the present vorticity-free method (i.e. spatial integration of the fluid potential in Eq. 12) is compared with a direct evaluation of this quantity from the DNS over the time interval $0.4T_S < t < T_S$, where T_S is the duration of the piston stroke. The agreement is very good. Since the numerical data set provides a vorticity field that is well resolved even near the solid boundaries, we can also compute the instantaneous first moment of vorticity in the flow in order to determine the fluid momentum by a vorticity approach (Wu 1981). This result is also close to the DNS calculation, as expected since the effect of nozzle exit overpressure, which may not be captured by the vorticity approach, has decayed by the time $t = 0.4T_S$.

As mentioned previously, the vorticity-free analyses implemented presently rely on the assumption that there is no vorticity on or external to the LCS boundary, so that the shear stresses on the LCS surface are negligible. This hypothesis can be tested directly based on the measured velocity field data, by integrating the shear stress tensor $\boldsymbol{\tau}$ on the surface $S(t)$ of the LCS and comparing this with the computed locomotive force $\mathbf{F}_\mathrm{L}$. The ratio $\frac{\int_S \boldsymbol{\tau}\cdot\mathbf{n}\,\mathrm{d}S}{\mathbf{F}_\mathrm{L}}$ is evaluated in Fig. 10 for DPIV measurements of the pectoral fin

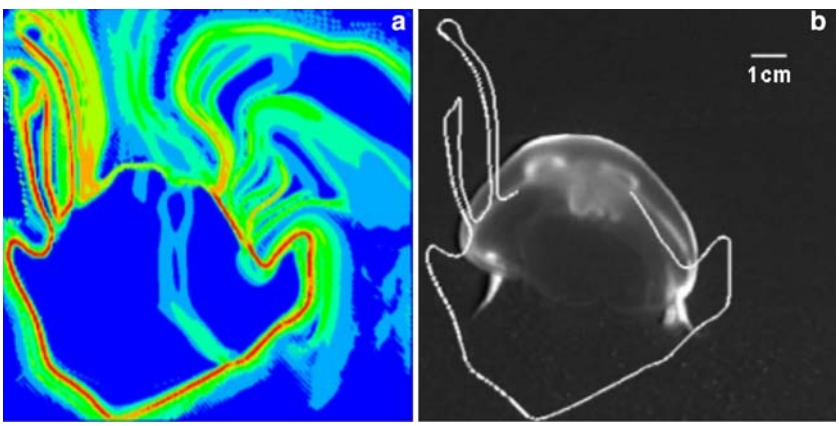

Fig. 5 **a** Shows the forward-time FTLE field of the flow around a free-swimming jellyfish. **b** Shows the LCS derived from the FTLE at the same instant. The image of the jellyfish is overlayed for reference

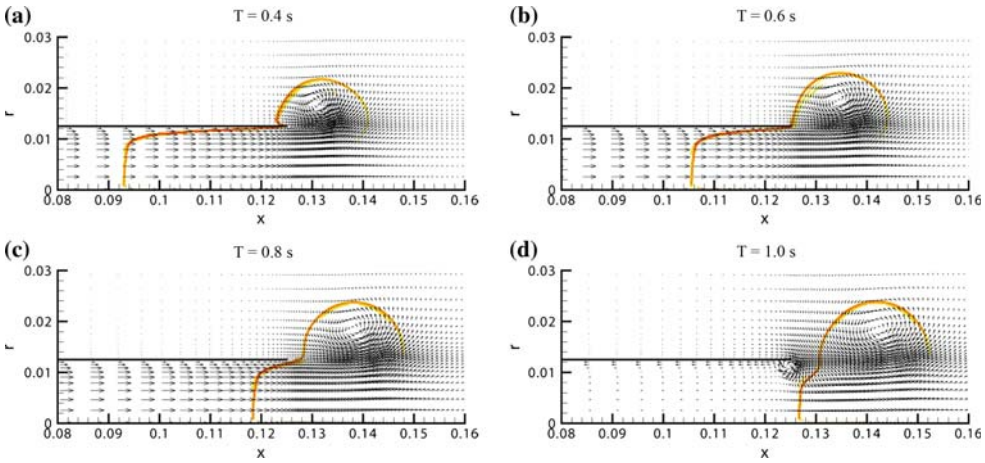

Fig. 7 Velocity field and the forward-time FTLE for direct numerical simulation of a vortex ring generated by a piston-cylinder apparatus. The longitudinal (x) and radial (r) axes are plotted in meters. The ridge of highest FTLE values is shown in *red*. The cylinder wall is indicated by the *black horizontal line*

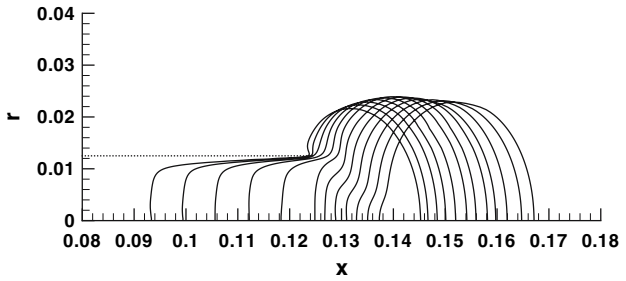

Fig. 8 Temporal evolution of the vortex boundary, shown as *solid lines*. The vortex moves from *left* to *right*. *Dotted line*: cylinder wall

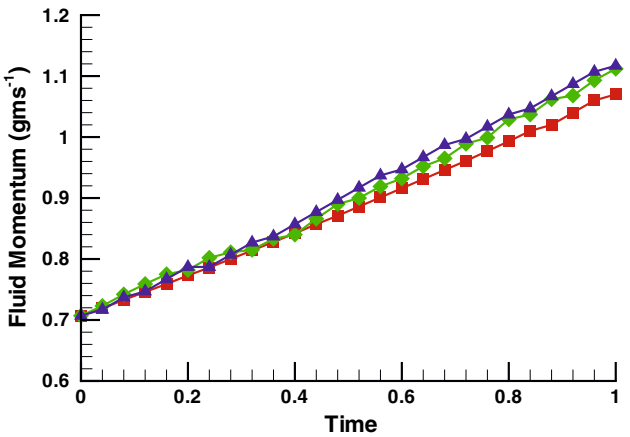

Fig. 9 Comparison of total fluid momentum. *Red squares*: direct DNS calculation; *green diamonds*: vorticity-free method; *blue triangles*: vorticity method. Time $t = 0$ corresponds to 0.4 normalized time units after flow initiation

and the free-swimming jellyfish from the previous sections. Figure 10 shows that in both cases the shear on the LCS is small relative to the locomotive force, consistent with the potential flow hypothesis. The local peak in the pectoral fin data is attributable to vorticity outside the dorsal edge of the LCS, as seen in Fig. 3c. This vorticity external to the LCS causes the potential flow hypothesis to break down locally. The quantitative effect of non-compact vorticity on the validity of the potential flow hypothesis is an issue of ongoing study.

4 Discussion

The ability of the present methods to deduce unsteady fluid forces and moments makes them a valuable complement to existing techniques for quantitative studies of animal swimming. The vorticity-free approach can benefit from the wealth of theoretical tools developed for the study of potential flows, such as Hamiltonian formulations for optimization (e.g. Galper and Miloh 1995). From the perspective of an experimentalist, these methods possess the practical advantage that vorticity dynamics need not be resolved exactly. Furthermore, Haller (2002) showed that the geometry and kinematics of the LCS are robust to localized measurement errors (which will appear in the computed fluid particle trajectories), whereas the integrals that must be evaluated in common vorticity formulations are not.

To be sure, the present approach requires the extraction of fluid particle trajectories, data that we have derived here from Eulerian, DPIV data. In principle, it would be more efficient to extract these trajectories empirically, as in particle-tracking velocimetry (PTV) techniques. However, PTV methods are most effective in flows with relatively low seeding densities, typically at least an order of magnitude less than DPIV. Computing the FTLE fields would then require substantial interpolation of the measured fluid particle trajectories. One potential advantage of this approach, however, is that three-dimensional PTV can be implemented with substantially greater ease than an equivalent DPIV technique. Furthermore, PTV has experienced significant refinements recently (Pereira et al. 2006; Ouellette et al. 2006). The extraction of three-dimensional fluid

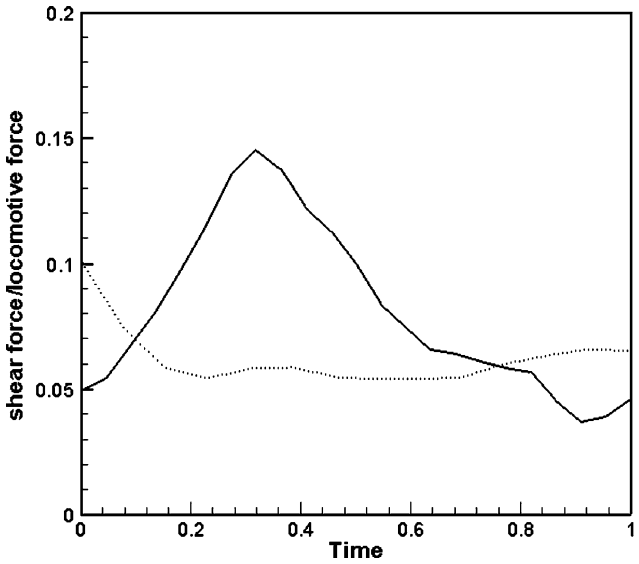

Fig. 10 Ratio of the shear force on LCS surface to the magnitude of the locomotive force. *Solid line*: bluegill sunfish pectoral fin; *dotted line*: free-swimming jellyfish

dynamics from animal swimming measurements may be facilitated by the use PTV within the context of a Lagrangian, vorticity-free method of analysis.

Perhaps the greatest challenge for animal swimming measurements lies in quantitative validation of the results. Fluid dynamic force and moment measurements cannot usually be validated directly in these cases; at best, they can be shown consistent with known requirements for locomotion of a particular animal (e.g. balancing negative buoyancy) or with measured body kinematics (i.e. linear and angular position, velocity and acceleration). Simultaneous measurements of body and flow kinematics will ultimately be required in order to confirm the conclusions of fluid dynamic studies currently being undertaken in the field.

Finally, we reiterate that the methods developed here are very general. Immediate applications of this vorticity-free perspective to animal swimming can be found in studies of C- and S-starts; labriform, carangiform, and anguilliform locomotion; and jet propulsion. Animal flight can be studied under this same paradigm, as can bluff-body flows and fluid–structure interactions more broadly. The transport properties of LCS have recently been studied within the context of animal swimming (Franco et al. 2007), resulting in new physical insights into the coupling of mass and momentum transport during animal swimming.

Acknowledgments The authors are grateful for collaborations on this work with J.E. Marsden, S.C. Shadden, G.V. Lauder, P.G. Madden, M. Rosenfeld, E. Franco, D.N. Pekarek, and K. Katija. This research is supported by a grant from the Ocean Sciences Division, Biological Oceanography Program at NSF (OCE 0623475) to J.O.D.

References

Anderson EJ, McGillis WR, Grosenbaugh MA (2001) The boundary layer of swimming fish. J Exp Biol 204:81–102

Bartol IK, Gharib M, Webb PW, Weihs D, Gordon MS (2005) Body-induced vortical flows: a common mechanism for self-corrective trimming control in boxfishes. J Exp Biol 208: 327–344

Beal DN, Hover FS, Triantafyllou MS, Liao JC, Lauder GV (2006) Passive propulsion in vortex wakes. J Fluid Mech 549:385–402

Dabiri JO, Colin SP, Costello JH, Gharib M (2005) Flow patterns generated by oblate medusan jellyfish: field measurements and laboratory analyses. J Exp Biol 208:1257–1265

Daniel TL (1984) Unsteady aspects of aquatic locomotion. Am Zool 24:121–134

Drucker EG, Lauder GV (1999) Locomotor forces on a swimming fish: three-dimensional vortex wake dynamics quantified using digital particle image velocimetry. J Exp Biol 202:2393–2412

Drucker EG, Lauder GV (2001) Wake dynamics and fluid forces of turning maneuvers in sunfish. J Exp Biol 204:431–442

Franco E, Pekarek DN, Peng J, Dabiri JO (2007) Geometry of unsteady fluid transport during fluid-structure interactions (in press)

Galper A, Miloh T (1995) Dynamic equations of motion for a rigid or deformable body in an arbitrary non-uniform potential flow field. J Fluid Mech 295:91–120

Gopalkrishnan R, Triantafyllou MS, Triantafyllou GS, Barrett D (1994) Active vorticity control in a shear-flow using a flapping foil. J Fluid Mech 274:1–21

Green MA, Rowley CW, Haller G (2006) Detection of Lagrangian coherent structures in 3D turbulence. J Fluid Mech 572:111–120

Haller G (2000) Finding finite-time invariant manifolds in two-dimensional velocity fields. Chaos 10:99–108

Haller G (2001) Distinguished material surfaces and coherent structures in three-dimensional fluid flows. Physica D 149:248–277

Haller G (2002) Lagrangian coherent structures from approximate velocity data. Phys Fluids 14:1851–1861

Lamb H (1932) Hydrodynamics. Dover, New York

Liao JC, Beal DN, Lauder GV, Triantafyllou MS (2003) Fish exploiting vortices decrease muscle activity. Science 302:1566–1569

Noca F, Shiels D, Jeon D (1997) Measuring instantaneous fluid dynamic forces on bodies, using only velocity fields and their derivatives. J Fluid Struct 11:345–350

Noca F, Shiels D, Jeon D (1999) A comparison of methods for evaluating time-dependent fluid dynamic forces on bodies, using only velocity fields and their derivatives. J Fluid Struct 13:551–578

Ouellette NT, Xu HT, Bodenschatz E (2006) A quantitative study of three-dimensional Lagrangian particle tracking algorithms. Exp Fluids 40:303–313

Peng J, Dabiri JO (2007) An overview of a Lagrangian method for analysis of animal wake dynamics. J Exp Biol (in press)

Peng J, Dabiri JO, Madden PG, Lauder GV (2007) Non-invasive measurement of instantaneous forces during aquatic locomotion: a case study of the bluegill sunfish pectoral fin. J Exp Biol 210:685–698

Pereira F, Stuer H, Graff EC, Gharib M (2006) Two-frame 3D particle tracking. Meas Sci Tech 17:1680–1692

Shadden SC (2006) A dynamical systems approach to unsteady systems. Ph.D. Thesis, California Institute of Technology

Shadden SC, Lekien F, Marsden JE (2005) Definition and properties of Lagrangian coherent structures from finite-time Lyapunov exponents in two-dimensional aperiodic flows. Physica D 212:271–304

Shadden SC, Dabiri JO, Marsden JE (2006) Lagrangian analysis of entrained and detrained fluid in vortex rings. Phys Fluids 18:047105

Shadden SC, Katija K, Rosenfeld M, Dabiri JO, Marsden JE (2007) Transport and stirring induced by vortex formation (submitted)

Stamhuis EJ, Nauwelaerts S (2005) Propulsive force calculations in swimming frogs. II. A vortex ring approach. J Exp Biol 208:1445–1451

Wilga CD, Lauder GV (2004). Biomechanics: hydrodynamic function of the shark's tail. Nature 430:850

Wu JC (1981) Theory for aerodynamic force and moment in viscous flows. AIAA J 19:432–441